Nonlinear simulations of combustion instabilities with a quasi-1D Navier–Stokes code

Nils Erland L. Haugen *, Øyvind Langørgen, Sigurd Sannan

SINTEF Energy Research, NO-7465 Trondheim, Norway

A R T I C L E   I N F O

A B S T R A C T

As lean premixed combustion systems are more susceptible to combustion instabilities than non-premixed systems, there is an increasing demand for improved numerical design tools that can predict the occurrence of combustion instabilities with high accuracy. The inherent nonlinearities in combustion instabilities can be of crucial importance, and we here propose an approach in which the one-dimensional (1D) Navier–Stokes and scalar transport equations are solved for geometries of variable cross-section. The focus is on attached flames, and for this purpose a new phenomenological model for the unsteady heat release from a flame front is introduced. In the attached flame method (AFM) the heat release occurs over the full length of the flame. The nonlinear code with the use of the AFM approach is validated against analytical results and against an experimental study of thermoacoustic instabilities in oxy-fuel flames by Ditaranto and Hals [Combustion and Flame 146 (2006) 493–512]. The numerical simulations are in accordance with the experimental measurements and the analytical results and both the frequencies and the amplitudes of the resonant acoustic pressure modes are reproduced with good accuracy.

1. Introduction

New and stricter emission regulations, particularly on nitrogen oxides, have led to the adoption of lean premixed combustion as the primary technology for low-emission power generation from gaseous fuels in stationary gas turbines. Homogeneous premixing of the fuel and the oxidizer, combined with an ultra-lean operation mode, provide for lower combustion temperatures and a drastic reduction in NO_x formation, accompanied by lower emission of soot and CO. Experience has shown, however, that lean premixed combustion systems are more susceptible to combustion instabilities than non-premixed systems. The coupling between unsteady heat release and acoustic pressure oscillations can lead to self-excited oscillations that cause unacceptable levels of noise and moreover tend to reduce combustion efficiency. These thermoacoustic oscillations also have a detrimental effect on the combustor equipment that limits the component lifetime and, in the worst case, can result in system failure due to structural damage.

The thermoacoustic instabilities involve a feedback cycle in which the heat release rate and acoustic pressure fluctuations are coupled. A stability criterion was deduced by Lord Rayleigh [1], which states that the pressure wave will be amplified and develop an instability if the heat release fluctuations are in phase with the acoustic pressure oscillations. Oppositely, the system is stable if the heat release rate and acoustic pressure fluctuations are out of phase. In general, there

---

* Corresponding author. Tel.: +47 73550675.
E-mail address: nils.e.haugen@sintef.no (N.E. Haugen).

are various types of combustion instabilities due to the different physical mechanisms that can drive the instability. The underlying driving mechanism depends on the combustor geometry, the burner and flame types, and the set-up of the fuel and oxidizer feed lines. Thus, an instability due to variation in the equivalence ratio may arise if the acoustics is able to interact with the upstream flow all the way to the individual feed lines. Another type of instability occurs if the acoustic pressure oscillations affect the incoming velocity of the fuel-oxidizer mixture into the flame front. Reviews of the acoustically coupled combustion instabilities, as well as other instability mechanisms that do not couple directly to the system acoustics, are given by Candel [2] and McManus et al. [3].

Combustion instabilities and the interactions between several different physical phenomena such as variations in the flow velocities, acoustic pressure fluctuations, and heat release are inherently complex by nature. Traditionally, combustion system designers have relied on experiments in order to obtain vital information for the design of combustors, where instabilities can be avoided or controlled. However, performing a series of large-scale experiments, in some cases under high pressure to create gas turbine operating conditions, is very costly. For this reason the development of numerical design tools based on computational fluid dynamics (CFD) has become an important endeavor in recent years in order to complement experiments in the design process. The complexity of the instability mechanisms and their interactions, however, places severe demands on both the physical modeling and the numerical analysis of current CFD techniques. Hence, the development of CFD as a reliable design and analysis tool with sufficiently high prediction accuracy with regard to combustion instabilities is an extremely challenging task.

The most accurate method to study turbulent combusting flows numerically is by direct numerical simulation (DNS), where the flow field is solved directly from the Navier–Stokes equations [4]. Due to the huge computational cost, however, the use of DNS is restricted to simplified problems and turbulent flows with relatively low Reynolds number. For high Reynolds number flows in complex geometries, as often encountered in industrial applications, DNS is therefore prohibitively expensive and is likely to be beyond reach for quite some time. A computationally less demanding approach is large eddy simulation (LES), in which the large turbulent eddies of the flow are computed explicitly, while the smaller eddies are not resolved but modeled using a subgrid scale model. LES is well suited to the description of unsteady dynamical phenomena, and there has been a growing interest in LES in recent years [5]. But even LES is limited due to expensive computational costs, and thus 3D LES calculations are non-practical for use on an everyday basis in industrial applications.

As a consequence of the complexity of instability mechanisms, much of the modeling work on combustion instabilities has focused on simplified models to make problems tractable. The development of linear models, in which the Navier–Stokes equations and scalar transport equations are linearized, has been a very useful approach capable of predicting combustion instabilities at a qualitative level [3]. Thus linear acoustic models can predict, at least to some extent, the frequencies of resonant modes and their growth rate during a phase of exponential growth. A current practice in the modeling of unstable combustion systems is to apply a network model, where the geometry of the combustor is modeled by a network of acoustic elements and a simplified form of the pressure equation is solved. The acoustic elements of a network model, also called multiports, correspond to various components of the system, e.g., the air or fuel supply, the transition between two regions of different cross-section, the outlet of the combustor, or the flame itself [6–10]. Mathematically, each multiport in the system is represented by a transfer function.

Although the predictive scope of linear models is limited, the use of linear models for active control of combustion instabilities has been widespread [3,11]. However, linear models are not able to predict the amplitudes of the resonant modes of the statistically stationary state, and hence the dominating instabilities of the system cannot be distinguished from the less significant ones. Also, the couplings between the instability mechanisms may not be accurately represented in linear models and there has therefore been a growing interest in active control based on nonlinear models [12]. When the nonlinear Navier–Stokes and scalar transport equations are solved, it is possible to predict the shape and the level of the acoustic frequency spectrum both during the exponential growth phase and for the statistically stationary state. This should make for a more accurate and efficient active control of the combustion instabilities. In a nonlinear real-space description it is furthermore possible to apply more reliable models for the heat release, as discussed in Section 4.2. An alternative approach to solving the nonlinear real space equations is to solve a nonlinear wave equation in the frequency domain [13,14].

In this paper we have chosen an approach where the nonlinear Navier–Stokes and scalar transport equations are solved for a combusting flow in real space and time, as in a DNS or an LES, but in a reduced 1D description. Previous work on real-space 1D nonlinear CFD simulations of combustion instabilities includes the work of Polifke et al. [10] and Rook [15]. Polifke et al. [10] considered thermoacoustic oscillations in a straight duct by introducing a 1D heat release model for a heat source placed in the duct. From time-dependent simulations of the dynamical behavior of the heat source, the authors were able to obtain the transfer matrix of the heat source which again could be investigated in a linear network model. Rook [15] applied 1D CFD to study the acoustical behavior of a burner-stabilized flame using a pressure correction method to simulate the flame on a ceramic foam burner. We here follow the approach of variable cross-section area introduced by Cohen et al. [16], and also used by Prasad and Feng [17,18], where the 1D equations are written for variable-area geometries in order to simulate 3D geometries. The reduction of the governing equations to 1D is valid for relatively simple geometries for which the flow can be assumed to be quasi-1D, and where the wavelengths are sufficiently large, so that the wave motion is well approximated by a plane wave. In this framework we propose a new phenomenological model for the unsteady heat release from a flame front. The flame model, here termed as the attached flame method

(AFM), gives a 1D realization of the flame front. Using AFM it is demonstrated that the 1D simulations capture both the exponential growth and the nonlinear statistically stationary state of the acoustic oscillations at a computational cost far below that of a corresponding DNS or an LES.

In Section 2, we present the governing equations, and make them 1D by introducing a variable cross-section. Boundary conditions is discussed in Section 3, while the new flame model is described in Section 4. Finally, the code is verified in Section 5 by comparing the simulation results with experimental results from a study of combustion instabilities in oxy-fuel flames by Ditaranto and Hals [19].

2. The governing equations

The governing equations for a turbulent combusting flow are based on the conservation of mass, momentum and energy, and the transport equations for species mass fractions. The conservation of mass is represented by the continuity equation

$$\frac{\partial \rho}{\partial t} + \nabla \cdot \rho \mathbf{u} = 0, \tag{1}$$

while the conservation of momentum gives the Navier–Stokes equations

$$\rho \frac{\partial \mathbf{u}}{\partial t} + \rho \mathbf{u} \cdot \nabla \mathbf{u} = -\nabla p + \nabla \cdot \boldsymbol{\tau}, \tag{2}$$

where ρ is the density, $\mathbf{u}$ is the velocity vector, p is the pressure, and $\boldsymbol{\tau}$ is the viscous stress tensor. For a Newtonian fluid the stress tensor is given by $\boldsymbol{\tau} = 2\mu \mathbf{S}$, where μ is the dynamic viscosity, and $\mathbf{S}$ is the traceless strain tensor with components[1]

$$S_{ij} = \frac{1}{2}\left(\frac{\partial u_i}{\partial x_j} + \frac{\partial u_j}{\partial x_i} - \frac{2}{3} \delta_{ij} \frac{\partial u_k}{\partial x_k} \right), \tag{3}$$

when we use the Einstein summing convention. The conservation equation for the energy can be rewritten in terms of the temperature equation

$$\rho \frac{\partial T}{\partial t} + \rho \mathbf{u} \cdot \nabla T = \frac{1}{c_v}(-p\nabla \cdot \mathbf{u} + \nabla \cdot (\lambda \nabla T) + \dot{q}_v + \dot{q}_c), \tag{4}$$

where T is the temperature, c_v is the specific heat at constant volume, λ is the thermal conductivity, $\dot{q}_v = 2\mu \mathbf{S}^2$ is the viscous heating source term, and $\dot{q}_c$ is the heat release rate from combustion. The equations for the mass fractions Y_k of the species k can be written as

$$\rho \frac{\partial Y_k}{\partial t} + \rho \mathbf{u} \cdot \nabla Y_k = \nabla \cdot (\rho D \nabla Y_k) + \rho \omega_k, \quad k = 1, \ldots, N_S, \tag{5}$$

where D is the mass diffusivity, ω_k is the chemical reaction rate of species k, and N_S is the number of species. The above set of equations are closed via the ideal gas equation of state

$$p = \rho r T, \tag{6}$$

where r is the gas constant of the mixture. The mixture gas constant is given by $r = R/\overline{m}$, where $R = 8.31$ kJ/(kmol K) is the universal gas constant, and $\overline{m}$ is the mean molar mass. The speed of sound in the gas mixture is

$$c_0 = \sqrt{\gamma r T}, \tag{7}$$

where $\gamma = c_p/c_v$ is the specific heat ratio, with c_p the specific heat constant pressure.

2.1. The variable cross-section 1D approximation

In a variable cross-section geometry the combusting flow can be solved by a quasi-1D treatment. The reduced governing equations in 1D are presented here. In a quasi-1D description the traceless strain tensor is reduced to

$$\mathbf{S} = \mathrm{diag}\left(\frac{2}{3}, -\frac{1}{3}, -\frac{1}{3} \right) \frac{\partial u}{\partial x}. \tag{8}$$

From this it follows that the viscous force is

$$\nabla \cdot \boldsymbol{\tau} = \nabla \cdot (2\nu\rho \mathbf{S}) = \frac{4}{3}\mu\left(\frac{\partial^2 u}{\partial x^2} + \frac{\partial u}{\partial x}\frac{\partial \ln \rho}{\partial x} \right), \tag{9}$$

---

[1] The bulk viscosity has been set to zero by Stokes' hypothesis.

where μ is the dynamic viscosity. Furthermore, the viscous heating reduces to

$$\dot{q}_v = 2\mu \mathbf{S}^2 = \frac{4}{3}\mu\left(\frac{\partial u}{\partial x}\right)^2. \tag{10}$$

It should be noted that the factor 4/3 in the above equations is due to the 1D approximation.

The quasi-1D continuity equation for a variable cross-section geometry can be written as

$$\frac{\partial \rho}{\partial t} = -\frac{1}{A}\frac{\partial \rho A u}{\partial x}, \tag{11}$$

where A is the cross-sectional area. It follows that the 1D equations for the momentum, the temperature and the species mass fractions are given by

$$\frac{\partial u}{\partial t} = -u\frac{\partial u}{\partial x} - \frac{1}{\rho}\frac{\partial p}{\partial x} + \frac{4}{3}\nu\left(\frac{\partial^2 u}{\partial x^2} + \frac{1}{\rho}\frac{\partial u}{\partial x}\frac{\partial \rho}{\partial x}\right) + \frac{F_{f,w}}{\rho}, \tag{12}$$

$$\frac{\partial T}{\partial t} = -u\frac{\partial T}{\partial x} + \frac{1}{\rho c_v}\left(-\frac{p}{A}\frac{\partial u A}{\partial x} + \frac{\partial}{\partial x}\left(\lambda\frac{\partial T}{\partial x}\right) + \dot{q}_v + \dot{q}_c + \dot{q}_{v,w}\right) \tag{13}$$

and

$$\frac{\partial Y_k}{\partial t} = -u\frac{\partial Y_k}{\partial x} + \frac{1}{\rho}\frac{\partial}{\partial x}\left(\rho D\frac{\partial Y_k}{\partial x}\right) + \omega_k, \tag{14}$$

where $F_{f,w}$ represents the viscous force from the walls, and $\dot{q}_{v,w}$ is the corresponding viscous heating. These terms are added to the system since the viscous force in Eq. (9) contributes to damping in the streamwise direction only, i.e., wall effects do not naturally appear in the 1D equations. For more information on the viscous force $F_{f,w}$, see Appendix A. If the viscous wall effects are negligible, $F_{f,w}$ and $\dot{q}_{v,w}$ in Eqs. (12) and (13) can be set to zero.

Numerically, the set of equations (11)–(14) are solved using an explicit solver. The spatial discretization is sixth-order finite difference, while third-order Runge–Kutta is used for the time stepping.

3. Boundary conditions

3.1. Open boundaries

We assume that the time varying pressure and velocity field in the system can be decomposed as

$$p = p_0 + p',$$

$$u = u_0 + u', \tag{15}$$

where subscript 0 denotes the mean part while prime denotes the fluctuating part. In addition, the density fluctuations ρ' are given by

$$\rho = \rho_0 + \rho', \tag{16}$$

where ρ_0 is the average density. The acoustic pressure fluctuations are described by plane harmonic waves given by

$$p' = \hat{p}e^{-i\omega t} = (A^+ e^{ikx} + A^- e^{-ikx})e^{-i\omega t}, \tag{17}$$

where $k = 2\pi/\lambda$ is the wavenumber, ω is the angular frequency, and A^+ and A^- denote the amplitudes of the right-moving and left-moving pressure waves, respectively. Similarly, the velocity fluctuations are given by

$$u' = \hat{u}e^{-i\omega t} = \frac{1}{\rho_0 c_0}(A^+ e^{ikx} - A^- e^{-ikx})e^{-i\omega t}. \tag{18}$$

In a long duct with an open exit at $x=0$, the impedance at the exit is

$$Z = \frac{\hat{p}}{\hat{u}} = \rho_0 c_0\left(\frac{A^+ + A^-}{A^+ - A^-}\right) = \rho_0 c_0\left(\frac{1-R}{1+R}\right), \tag{19}$$

where the reflection coefficient R is defined by $R = -A^-/A^+$. Rearranging the above equation we get

$$R = \frac{\rho_0 c_0 - Z}{\rho_0 c_0 + Z}. \tag{20}$$

We notice that if $Z=0$ there is perfect reflection and $R=1$. If $Z = \rho_0 c_0$, corresponding to the characteristic impedance of the medium, $R=0$ and there is no reflection at the exit. Since $p'/u' = \hat{p}/\hat{u} = Z$, we may use the equation of state (6), together with Eq. (19), to write

$$p' = \rho r T - p_0 = Z u' = \rho_0 c_0\left(\frac{1-R}{1+R}\right)(u - \overline{u}). \tag{21}$$

Solving this equation with respect to the temperature, we obtain

$$T = \frac{1}{\rho r}\left(p_0 + \rho_0 c_0 (u-\overline{u})\left(\frac{1-R}{1+R}\right)\right). \tag{22}$$

Thus, at an open boundary the temperature is determined by the expression (22).

3.1.1. Reflection coefficients at open boundaries

We consider acoustic oscillations in long ducts. If the duct is a circular pipe, the characteristic Helmholtz number is defined as $H_n = ka$, where a is the radius of the pipe. Thus, the Helmholtz number is small if the pipe radius is small compared to the acoustic wavelength. It is known that for low Helmholtz numbers the dominating acoustic modes within a pipe will be reflected from an open end, i.e., most of the acoustic energy will not leave the pipe [20]. This is normally also the condition for combustion instabilities to appear. By assuming that $H_n \ll 1$ and applying conservation of mass, it has been shown that the absolute value of the reflection coefficient at the open end of an unflanged pipe is [21]

$$|R| = 1 - \tfrac{1}{2}(ka)^2, \quad ka < 0.2. \tag{23}$$

For large acoustic velocities $\hat{u}$, nonlinear effects at the exit will no longer be negligible. The dominating nonlinearity being the vortex shedding at the sharp bends of the exit. Peters et al. [21] find the acoustic power absorbed by vortex shedding, and non-dimensionalized by $P_{\mathrm{norm}} = \tfrac{1}{2}\rho\hat{u}^3\pi a^2$, to be

$$P_{\mathrm{vortex}}^* = \frac{P_{\mathrm{vortex}}}{P_{\mathrm{norm}}} = \beta \mathrm{Sr}_{ac}^{1/3}, \tag{24}$$

for the acoustic Strouhal number $\mathrm{Sr}_{ac} = \omega a/\hat{u} \gg 1$, and

$$P_{\mathrm{vortex}}^* = \frac{2c_d}{3\pi}, \tag{25}$$

for $\mathrm{Sr}_{ac} \ll 1$. In the above $c_d = 2$ for an unflanged pipe and we have set $\beta = 0.5$ in the simulations.

If Re(Z) is the real part of the impedance Z, the power lost at the outlet due to radiation from the pipe exit can be found by using Eqs. (19) and (23) to be

$$P_{\mathrm{rad}} = \pi a^2 I = \pi a^2 \tfrac{1}{2}\mathrm{Re}(Z)|\hat{u}|^2, \tag{26}$$

where I is the intensity. This gives

$$P_{\mathrm{rad}}^* = \frac{P_{\mathrm{rad}}}{\frac{1}{2}\rho\hat{u}^3\pi a^2} = \tfrac{1}{4}ka\mathrm{Sr}_{ac}. \tag{27}$$

Combining the above equations gives the following expression for the reflection coefficient as a function of the power loss

$$R = \frac{\frac{c_0}{\hat{u}} - P_{\mathrm{loss}}^*}{\frac{c_0}{\hat{u}} + P_{\mathrm{loss}}^*}, \tag{28}$$

when $P_{\mathrm{loss}}^* = P_{\mathrm{vortex}}^* + P_{\mathrm{rad.}}^*$ is the sum of the acoustic losses through radiation and vortex shedding.

3.2. Closed boundaries

Closed boundaries are understood as acoustically closed boundaries that reflect acoustic waves. Thus, closed boundaries can either be closed or open with respect to the mass flow. If there is no inflow (mass flow) across the acoustically closed boundary the velocity u, together with the derivatives $\partial\rho/\partial x$ and $\partial T/\partial x$, are set to zero. On the other hand, if there is inflow across the acoustically closed boundary, the mass flow is given a constant value (the velocity u has a non-zero constant value).

An acoustically closed boundary with inflow can be thought of as wall with several small holes, e.g., a porous plate. The holes are so small that they do not affect the reflecting abilities of the wall. However, they are large enough, so that the mass flow entering the domain is significant and is allowed to cross the boundary.

By setting $\partial T/\partial x = 0$, the closed boundary is adiabatic. This is not necessarily precisely correct but the error introduced by this assumption is expected to be of minor importance.

4. The flame model

In this section we obtain an expression for the combustion heat release term $\dot{q}_c$ in Eq. (13). We begin by describing the well-known $n-\tau$ formulation and show how it can be integrated into a Navier–Stokes solver. We then introduce a new phenomenological flame model which we refer to as the attached flame method (AFM).

4.1. The n−τ model for unsteady heat release

As a first approximation we apply the $n-\tau$ model, which provides a global description of the unsteady heat release rate associated with combustion instabilities. The heat release rate (energy per unit time) in the $n-\tau$ model is given by [3]

$$Q' = \frac{An\rho c_0^2}{\gamma - 1} u(x, t-\tau),$$ (29)

where A is the cross-section of the duct, n is the interaction index determining the coupling between the velocity and heat release fluctuations, and τ is the time lag between these fluctuations. The heat release rate per volume is

$$\dot{q}_c' = \frac{Q'}{AL_f} = \frac{n\rho c_v \gamma T}{L_f} u(x, t-\tau),$$ (30)

where L_f is the flame length, and we have made use of the relation (7).

The $n-\tau$ model was originally designed for linear wave-equation models for which the main focus has been on the heat release fluctuations and their coupling to the flow-field perturbations. For an implementation of the $n-\tau$ formulation in a CFD code based on the Navier–Stokes equations, the mean part of the heat release needs to be included as well. Thus, the total heat release rate per volume (the mean part plus the fluctuation) can be written as

$$\dot{q}_c = \rho c_v \left(h_c + \frac{n\gamma T}{L_f} u(x, t-\tau) \right),$$ (31)

where h_c is a constant heat source. Both the constant h_c and the unsteady heat release are in this approach non-zero only within the flame.

4.2. The attached flame method (AFM)

The $n-\tau$ formulation is primarily designed to be used with linear wave-equation models in the frequency domain. Although generalizations to nonlinear applications have been made, the $n-\tau$ model is not optimal for use in a nonlinear Navier–Stokes solver where the governing equations are solved in real space and time. Thus, in the $n-\tau$ model the heat release is limited to a point source. In addition, the time lag τ must be accounted for.

More detailed analysis of unsteady heat release from flame fronts have been based on studies of the dynamics and shape of anchored premixed flames [22,23]. Fleifil et al. [24] used a kinematic model to calculate the transfer function in the linear regime between heat release and upstream velocity oscillation of a premixed flame stabilized on the rim of a tube. The kinematic approach was later extended by Schuller et al. [25] by including convective effects of the flow modulations propagating upstream of the flame. In this paper we present a new phenomenological model for the unsteady heat release from an attached flame. The model, denoted the attached flame method (AFM), is similar to the analytical flame front model [24,25] in the sense that a real-time differential equation is solved to capture the kinematics of the thermoacoustic instabilities. However, while the kinematic model is based on the G-equation approach to determine the location of the flame front, in AFM the flame position is obtained directly from the equations for the species mass fractions. The basic idea is here to project the flame, which is essentially 2D, into a 1D description.

One advantage of the AFM approach, compared to the $n-\tau$ formulation, is that for laminar flames no free parameters such as n and τ need to be determined. In the AFM formulation, the full length L_f of the flame is defined as the distance from the inlet, where the flame is anchored, to the point where all the fuel is burned. The flame length L_f is therefore a dynamical variable that changes with time according to system oscillations.

The laminar flame speed is known to vary slightly with the position in a flame. Thus, the laminar flame speed will in general be different at the base of the flame, in the flame tip, and in the main body of the flame. The spatial variations in the flame speed are believed to have only minor effects on the flame front, however, and have been neglected in the following. A known constant laminar flame speed has been assumed in the current formulation, although this can easily be changed if the effects of a variable flame speed are expected to be significant.

For a combusting flow in a long duct we assume that the flame front can be represented by piecewise straight lines, as shown in Fig. 1. The total flame surface ΔA_i within a 1D grid cell is then given by

$$\Delta A_i = 2\Delta H_i d,$$ (32)

where d is the depth of the 1D grid cell, i.e., the size of the grid cell in the direction perpendicular to the paper plane. The flame front is here the interface between the fresh and the burned gas within a given 1D grid cell. Since the approach is 1D only, the flame front is not resolved by the 1D code but it is evident that the distance from the centerline to the flame front, denoted h_i, is proportional to the mean mass fraction Y_{fuel} of the fuel in the 1D grid cell. This can be written as

$$\frac{h_i}{h} = \frac{Y_{\text{fuel}}}{Y_{\text{fuel,inlet}}},$$ (33)

where $Y_{\text{fuel,inlet}}$ is the mass fraction of the fuel at the inlet. We note that the limiting cases of $h_i = h$ upstream of the flame anchor at x_f and $h_i = 0$ downstream of the flame tip are recovered from the above equation. Differentiating Eq. (33) we

obtain

$$\frac{dh_i}{dx} = \frac{dY_{\text{fuel}}}{dx} \frac{h}{Y_{\text{fuel,inlet}}}, \tag{34}$$

which, when setting $\Delta h_i = \Delta x dh_i/dx$, gives

$$\Delta H_i = \sqrt{\Delta x^2 + \Delta h_i^2} = \Delta x \sqrt{1 + \left(\frac{h}{Y_{\text{fuel,inlet}}} \frac{dY_{\text{fuel}}^i}{dx} \right)^2}. \tag{35}$$

In the above derivation we have used the fact that the mass fraction of the fuel outside the flame cone is zero (burned gas), while the mass fraction of the fuel inside the flame cone equals the mass fraction of the fuel at the inlet (fresh gas).

Since the flame front is always moving into the fresh gas, the reaction rate of the fuel within the flame is given by

$$R = \frac{\Delta A_i Y_{\text{fuel,inlet}} S_L f_T}{\Delta V}, \tag{36}$$

where S_L is the laminar flame speed, and ΔV is the volume of the grid cell. The reaction rate of the fuel is then given by

$$R_{\text{fuel}} = \begin{cases} 0, & x < x_f, \\ -\frac{2S_L Y_{\text{fuel,inlet}} f_T}{h} \sqrt{1 + \left(\frac{h}{Y_{\text{fuel,inlet}}} \frac{dY_{\text{fuel}}}{dx} \right)^2}, & x_f \leq x \leq x_f + L_f, \\ 0, & x > x_f + L_f, \end{cases} \tag{37}$$

where $f_T \geq 1$ is a constant accounting for the fact that the real flame speed might be larger than the laminar flame speed due to turbulence. In fact, f_T, quantifying the turbulence in the flame, is the only closure needed in the model. In the current work the focus is on laminar problems, however, and the model is here validated for laminar or weakly turbulent cases only, for which $f_T = 1$.

By construction the AFM does not allow for more than two flame fronts for any given downstream position. That is, the angle α_i between a given flame front segment and the normal to the wall, as illustrated by α_1 in Fig. 1, must satisfy the condition $0 < \alpha_i < 90°$. This means that the model will not be able to describe vortex roll-up for instance, and is therefore mostly suited to compact flames. This is a natural consequence of the model being 1D.

For a chemical reacting system with N_S species, the general equation for a chemical reaction can be written as

$$\sum_{k=1}^{N_S} v_k' A_k \rightarrow \sum_{k=1}^{N_S} v_k'' A_k, \tag{38}$$
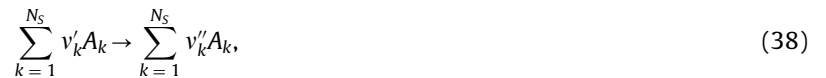
where A_k symbolizes the chemical species k, and v_k' and v_k'' are the stoichiometric coefficients of species k on the reactant and product side, respectively. The chemical reaction rate ω_k for such a system may be expressed as

$$\omega_k = (v_k'' - v_k') R_{\text{fuel}} \frac{m_k}{m_{\text{fuel}}}, \tag{39}$$

where m_k and m_{fuel} is the molar mass of species k and of the fuel, respectively.

The energy release within a grid cell is determined by the reaction rate R_{fuel} and the lower heating value h_L of the unburned mixture. Thus, the heat release term $\dot{q}_c$ in Eq. (13) is defined by

$$\dot{q}_c = R_{\text{fuel}} h_L \rho. \tag{40}$$

The expressions (39) and (40) are used to close the set of governing equations (11)–(14).
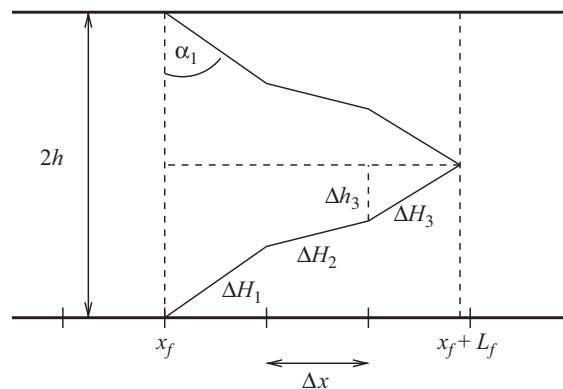

Fig. 1. In this duct of height $2h$ there is a flame holder at the position x_f in the streamwise direction. The flame front is represented by piecewise straight lines with total length $H = 2\sum \Delta H_i$, and the length of the flame is L_f. Every 1D grid cell has length Δx.
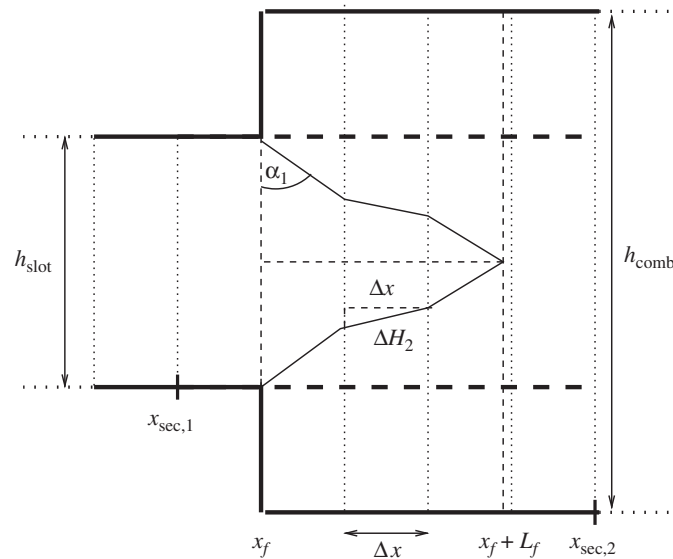
Fig. 2. The thick solid lines represent the geometry of a slot leading into a combustion chamber. The thick dashed line corresponds to the upper and lower boundary of the secondary grid within the chamber. The coordinates $x_{sec,1}$ and $x_{sec,2}$ define the boundaries of the secondary grid in the streamwise direction.

4.3. The secondary grid

In many applications of premixed combustion the geometry is such that a narrow slot leads into a wider combustion chamber. This is visualized in Fig. 2 where a slot of height h_{slot} leads into a combustion chamber of height h_{comb}. In such a geometry it is no longer correct to use the same convective velocity for the species convection in the jet as in the mean flow. The reason is that the *mean* convective velocity of the flow within the combustion chamber is lower than the convective velocity of the fresh fuel/air jet entering from the slot. Hence, we here solve the velocity evolution of the jet using a separate secondary subgrid. The jet entering the combustion chamber is visualized by the thick dashed lines in Fig. 2, which then also represent the upper and lower boundaries of the secondary grid within the chamber. Note, however, that since the simulation tool is formulated in 1D only, no boundary conditions are required at the dashed lines. In the streamwise direction the secondary grid is bounded by the coordinates $x_{sec,1}$ and $x_{sec,2}$, as shown in Fig. 2. In this subgrid domain the governing equations (11)–(14) are solved for a constant cross-section A and with no reactions, i.e., ω_k and $\dot{q}_c$ are both zero. This gives the convective velocity u_{conv} to be used in the convective term of Eq. (12). The secondary grid is thus applied to only a small fraction of the entire computational domain covered by the primary grid, which means that special care must be taken concerning boundary conditions. At the secondary subgrid inlet $x_{sec,1}$ the boundary values are chosen as the corresponding instantaneous values of the primary grid at the same location. For the subgrid outlet at $x_{sec,2}$ the non-reflecting boundary condition given by $R=0$ in Eq. (20) is used.

It should be pointed out that the matching of the secondary and the primary grid solutions in the above manner does not have any significant impact on the final results as long as both the inlet and the outlet of the secondary grid are outside the flame and a non-reflecting boundary condition is used at the secondary grid outlet.

5. Validation of the quasi-1D code

The nonlinear quasi-1D code is here validated against analytical, experimental and numerical results. We first compare with analytical results obtained in a simplified set-up of a flame in a duct. Next, numerical results for the flame transfer function obtained with AFM is compared with analytical results from a conical flame. Finally, the nonlinear code with the use of AFM is validated against results from an oxy-fuel study in a lab-scale test rig, both for inert and reactive flows.

5.1. Straight duct

We here consider a simplified case of a flame in a straight duct for which an analytical solution is known when the flame is described by the $n-\tau$ model. The AFM model is not applied in this particular case since a direct comparison between the AFM and $n-\tau$ model is not straightforward, given that various choices of n and τ may lead to very different physical solutions. Thus, the quasi-1D numerical results are here compared with the analytical solution given by Poinsot and Veynante [6], with the $n-\tau$ model applied in both approaches.

The simulated duct is assumed to be a straight pipe of length $2a$, where $a=0.5$ m and with the flame located in the center of the pipe. For the analytical treatment the heat source is a point source while for the nonlinear solver the flame has a length of 8 cm in the pipe direction. The spatial extension of the flame is required since any gradient or object in a spatial code must be resolved by at least a few grid points. The set-up is such that air enters at room temperature at the

pipe inlet. The constant heat source h_c given in Eq. (31) is chosen to be zero such that the mean temperature at the outlet equals the inlet temperature. The interaction index n between the velocity and the heat release is set to $n=0.25$.

First we will use the linear approximation, as described by Poinsot and Veynante [6], to find an analytical solution for the unstable frequencies and their growth rates. We are here primarily interested in the imaginary part of the frequency, which for this simplified case is given by

$$\text{Im}(\omega_j) = \frac{(-1)^j nc}{8\pi a} \sin(\omega_j \tau), \tag{41}$$

where c is the speed of sound, and

$$\omega_j = 2\pi f_j = (1+2j)\frac{2\pi c}{8a}. \tag{42}$$

In the linear approach the amplitude of the resonant mode j with frequency ω_j is given by $A_j = B_j \exp(-i\omega_j t)$, such that the amplitude A_j grows exponentially when the imaginary part of ω_j is positive. If the imaginary part of ω_j is negative, on the other hand, the amplitude of this particular mode will decay exponentially.

When simulating the same set-up as described above with the nonlinear quasi-1D simulation tool together with an $n-\tau$ flame model, one must consider the acoustic power spectrum in order to be able to compare with the results from the linear approach of Poinsot and Veynante [6]. These power spectra are represented by the solid lines in Fig. 3.

In Table 1, the imaginary parts of the first four ω_j's, as found from Eq. (41), are listed for three different values of τ. For $\tau = 6 \times 10^{-4}$ s it is evident that $\omega_1 = 1639$ Hz and $\omega_3 = 3824$ Hz are the unstable frequency modes. In the left plot of Fig. 3 the positions of these two modes are marked by large arrows, while the smaller arrows correspond to the decaying resonant modes. The solid line shows the acoustic power spectrum obtained from the numerical quasi-1D simulation, and it is seen that the excited modes agree well with the unstable modes as given by the analytical solution. In the last column of Table 1 the simulated growth rate is also found to be in good agreement with the theoretical values. For $\tau = 15 \times 10^{-4}$ s we note that the unstable frequency modes are given by $\omega_1 = 1639$ Hz and $\omega_2 = 2731$ Hz. In the middle plot of Fig. 3 we observe that the amplitude of ω_1 is much larger than the amplitude of ω_2, despite the fact that the imaginary part of ω_2 is larger than that of ω_1. This is because the initial perturbations were such that $B_1 \gg B_2$, and that the amplitude A_2, while still in the linear regime of the simulation, has not yet had enough time to catch up with A_1. This is also reflected by the fact that the simulated growth rate corresponds to the imaginary part of ω_1, implying that the dominating mode indeed is ω_1. Finally, for $\tau = 27 \times 10^{-4}$ s we find that there are no unstable frequency modes and that all the amplitudes are decaying. The resonant modes are nevertheless recovered in the right plot of Fig. 3, but the amplitudes are very weak (note the scale on the ordinate axis). For this case it should be noted that due to quite large uncertainties in the determination of the decay rate, the growth rate presented in Table 1 has relatively large error bars.

5.2. Flame transfer function

In this section numerical results for the flame transfer function obtained with AFM is compared with analytical results found by Schuller et al. [25]. The comparison is not expected to give an exact match as the current work
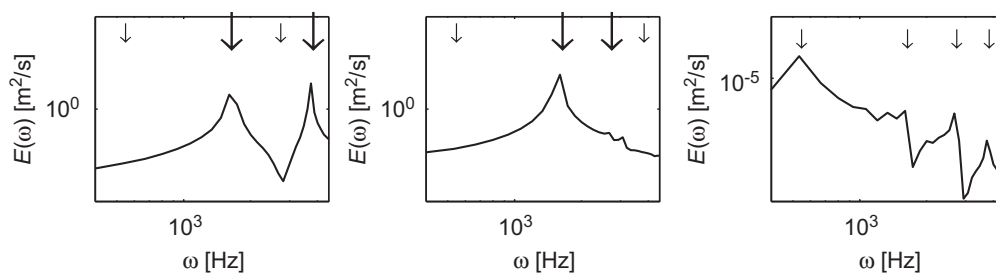

Fig. 3. Power spectra for simulations with $\tau = 6 \times 10^{-4}$ s (left), $\tau = 15 \times 10^{-4}$ s (middle), and $\tau = 27 \times 10^{-4}$ s (right). The solid line represents the simulated results while the arrows correspond to the resonant modes as found from Eq. (42). The larger arrows point at the unstable modes, while the smaller arrows give the decaying modes.

Table 1
Growth rate of unstable frequencies for different τ's. The angular frequencies are $\omega_0 = 546$ Hz, $\omega_1 = 1639$ Hz, $\omega_2 = 2731$ Hz, and $\omega_3 = 3824$ Hz. The $\text{Im}(\omega_i)$ are found from Eq. (41).

τ $(10^{-4}$ s$)$	$\text{Im}(\omega_0)$	$\text{Im}(\omega_1)$	$\text{Im}(\omega_2)$	$\text{Im}(\omega_3)$	Simulated growth rate
6	−2.2	5.8	−6.9	5.2	5.2
15	−5.1	4.4	5.7	−3.6	4.3
27	−6.9	−6.6	−6.2	−5.4	−5.6

is for a slot burner, while Schuller et al. [25] considered a conical flame. The results should nevertheless be qualitatively comparable.

Given a duct with cross-section $2h$ and a non-reflecting outlet on one side and an oscillating velocity inlet on the other side the flame transfer function can be found. Here the set-up of Schuller et al. [25] is followed such that the non-dimensional frequency is defined as

$$\omega_* = \frac{4h\omega}{S_L(1-(S_L/\overline{u})^2)^{1/2}},$$
(43)

where $\overline{u}$ is the mean inlet velocity. Please note the term $4h$ in the above equation has replaced the radius R used by Schuller et al. [25]. The flame transfer function is

$$F = \frac{q'/\overline{q}}{\dot{m}'/\overline{\dot{m}}},$$
(44)

where q is the heat release, $\dot{m} = \rho u$ is the mass flow rate, and the prime denotes fluctuating values around the means, represented by overbars. For weak acoustic waves $\rho' \ll \overline{\rho}$ such that $F \approx q'\overline{u}/\overline{q}u'$. Using the latter version of the flame transfer function for strong acoustic waves could cause the unphysical effect [29] of super unity gain for low frequencies, it is therefore recommended to always try to use the flame transfer function based on the mass flow rate and not on the velocity.

For a uniformly perturbed wave Schuller et al. [25] found the following analytical expression for the flame transfer function:

$$F = \frac{2}{\omega_*^2}[1-\exp(i\omega_*)+i\omega_*].$$
(45)

In Fig. 4, the absolute value of the analytical expression of Eq. (45) and the results found from simulations using AFM are compared. We note that the quasi-1D/AFM results presented in Fig. 4 are similar in appearance to what was found in the experiments of [26].

5.3. Sudden expansion burner

In this section we validate the nonlinear quasi-1D code against experimental results from the oxy-fuel study of Ditaranto and Hals [19]. A schematic view of the geometry of the lab-scale combustion rig is shown in Fig. 5. The set-up consists of a 80 cm long premixing section, followed by a 4 cm long flame arrestor and a 10 cm long slot leading into the 47.9 cm long combustion chamber. The premixing and combustor sections are square channels with cross-section $s \times s$, where $s = 5.4$ cm is the inner width of the sections. For the flame arrestor and the slot the cross-sections are $s \times d_{arr.}$ and $s \times d_{slot}$, respectively, where $d_{arr.} = 2$ cm and $d_{slot} = 0.5$ cm.

5.3.1. The cold rig

In order to validate the non-reactive part of the nonlinear code, acoustic simulations were performed for the geometry of the oxy-fuel rig described in [19], with no flame and only air present in the rig. Experimentally, in the cold rig case a loudspeaker was placed at the upstream end of the premixer, i.e., at the inlet at the left-end side of the set-up shown
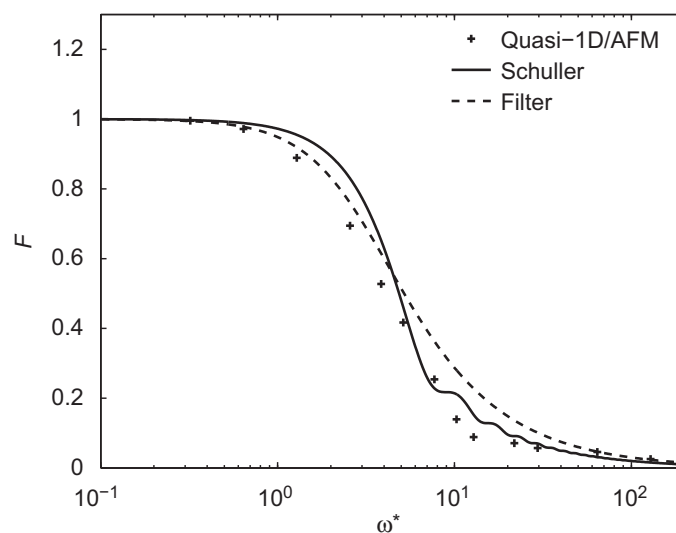

Fig. 4. The gain of the flame transfer function as a function of the non-dimensional frequency. The '+' signs represent the results found with the quasi-1D solver, the solid line is given by Eq. (45), while the dashed line is the first-order filtered form given by $f = 1 + i\omega_*/3$.
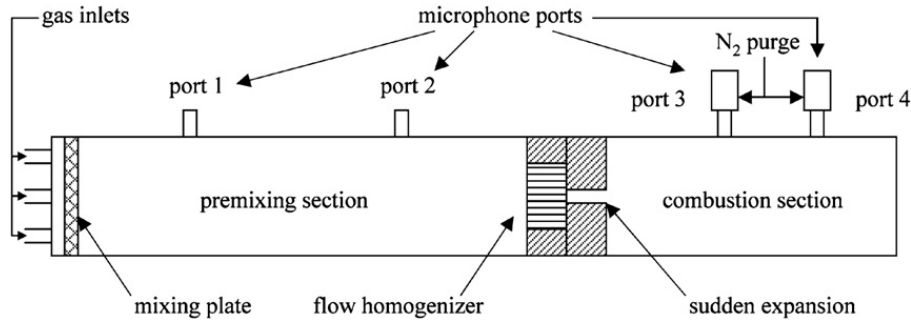
Fig. 5. Schematic view of the geometry of the oxy-fuel combustion rig used in the experimental study of Ditaranto and Hals [19].
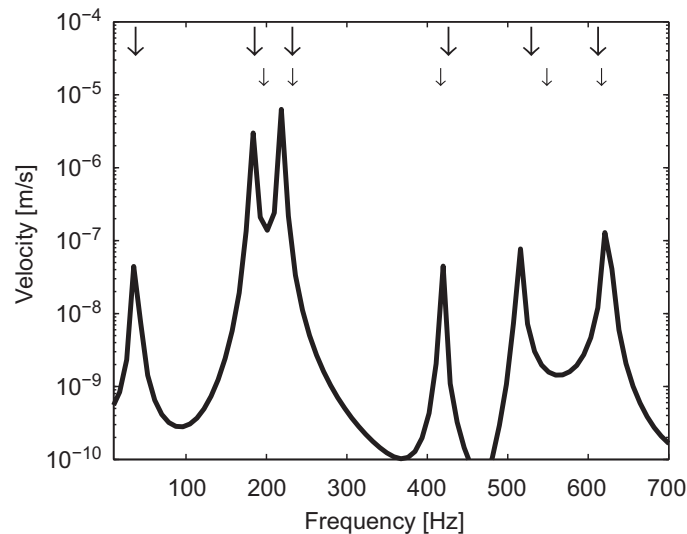

Fig. 6. The cold flow velocity spectrum from microphone port 3 of the rig illustrated in Fig. 5. The solid curve shows the spectrum obtained from the nonlinear code. The upper arrows indicate the measured resonant frequencies, while the lower (smaller) arrows indicate the resonances obtained from the linear code.

in Fig. 5. The acoustic frequency response of the loudspeaker was measured with four microphones, and for this procedure there was no flow in the system. The loudspeaker additionally produced white noise for which the spectral distribution is not known. The numerical simulations can therefore not reproduce the amplitudes of the resonant modes, but merely aim at reproducing the resonant frequencies.

The velocity spectrum corresponding to the statistically steady-state solution of the nonlinear code is plotted in Fig. 6. Also shown in this figure are the experimentally measured values of the resonant frequencies, along with the resonant frequencies obtained with the use of the linear code. We note that there is generally a good match between the measured resonant modes and those obtained by the numerical simulations. The resonant peak at ~ 25 Hz corresponds to the low frequency 1/4 mode of the entire system.

5.3.2. Oxy-fuel combustion

We here validate the full quasi-1D nonlinear code using the AFM formulation against an experimental study of combustion instabilities in oxy-fuel flames in a sudden expansion test rig. In the oxy-fuel study of Ditaranto and Hals [19] four different combustion instability regimes, referred to as regions, were distinguished. In Fig. 7, typical spectral distributions obtained in the oxy-fuel experiment for two of these regions are shown. The shown pressure spectra were recorded at microphone port 3 illustrated in Fig. 5. In what is referred to as Region 3 the flame front is attached to the slot of the rig at all times. For Region 2 the oxy-fuel flame study exhibited two instability patterns; one for which the flame is not attached to the slot but follows the formation of periodic large vortices, and another corresponding to a hysteresis phenomenon for which there is a combination of an attached flame branch and vortex shedding.

We observe from the spectral distributions of Fig. 7 that the instability frequencies are quite different for the shown cases. Thus, for the attached flame of Region 3 the 1/4 mode from the combustion chamber is at a significantly lower frequency (~ 230 Hz) than the corresponding modes (~ 300 Hz) for the cases in Region 2. According to Ditaranto and Hals [19], the instability frequency for the attached flame case is in fact a combination of the premixer 1/2 mode and the combustion chamber 1/4 mode. The premixer 1/2 modes for the cases of Region 2 both have frequencies at ~ 200 Hz,
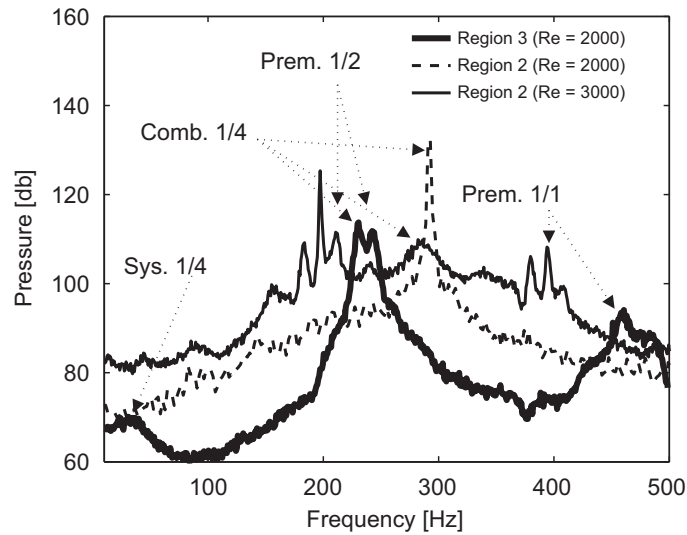
Fig. 7. The spectral distributions of pressure oscillations in the oxy-fuel rig as measured by Ditaranto and Hals [19]. The pressure spectra were recorded at microphone port 3 of the rig in two different instability regions. In Region 3 (thick solid line) the flame is attached to the slot. In Region 2 there are two instability patterns; one (thin solid line) displaying periodic vortex shedding and another (thin dashed line) being an intermediate case with both an attached flame branch and the formation of periodic vortices. The left arrow in the figure points to the low-frequency 1/4 mode of the entire system, the three next arrows point to the frequency peaks of the combustor 1/4 mode, the two upper arrows point to the peaks of the premixer 1/2 mode, while the two arrows to the right point to the frequency peaks of the 1/1 mode of the premixer.

although the mode corresponding to the hysteresis case is not dominant and difficult to observe in Fig. 7. Similarly, the premixer 1/1 modes for the cases of Region 2 have frequencies at ~ 400 Hz, while the corresponding mode of the attached flame case is at ~ 460 Hz. The main difference between the two instability cases of Region 2 is that the premixer 1/2 mode is most amplified when the flame follows the shedded vortices entirely, while the combustor 1/4 mode is dominant when the flame is partially attached to the slot.

The combustion chamber temperature was not measured by Ditaranto and Hals [19] and we therefore use the frequency peak of the ground mode of the combustor to estimate the average temperature. From Fig. 7 we note that the 1/4 mode of the combustion chamber is at a frequency $f_0 \approx 230$ Hz for the attached flame. We first compute the speed of sound and recall that the combustor has length 47.9 cm. For a duct with an open end we also know that the acoustics depends on an end correction to the duct length. For an open end unflanged pipe, Davies et al. [30] have obtained an empirical fit to the end correction given by

$$l/a = 0.6133 - 0.1168(ka)^2, \quad ka < 0.5, \tag{46}$$

where a is the radius of the pipe. For the square combustion duct we set $a = s/\sqrt{\pi} = 3.0$ cm, corresponding to a pipe of equal cross-section as the duct. This gives a length correction of $l \approx 1.8$ cm for the ground mode. Adding this to the combustor length, we find the acoustic length of the combustor to be $l_{acoustic} = (0.479 + 0.018)$ m $= 0.497$ m. With $f_0 = c_0/\lambda$ and $\lambda = 4l_{acoustic}$ for the 1/4 wave mode, this gives the average speed of sound in the combustion chamber

$$c_0 = 4f_0 l_{acoustic} = 458 \text{ m/s}. \tag{47}$$

Using Eq. (7), the average temperature in the combustion chamber then becomes

$$T = \frac{c_0^2}{\gamma r} = 720 \text{ K}, \tag{48}$$

where $\gamma = 1.24$ and $r = 235$ J/(kg K) for the given gas mixture. The average temperature is thus much lower than the adiabatic flame temperature at about 2400 K (when assuming a combustor inlet temperature of 400 K). In the following, we therefore allow for sufficient cooling in the combustion chamber such that the mean temperature downstream of the flame is 720 K.

As discussed in Section 4.2 the AFM model is not able to describe vortex roll-up but is designed to describe attached compact flames. For the validation of the quasi-1D code a numerical simulation of the case for which the flame was attached to the slot has therefore been performed. The case is typical of the instability regime of Region 3, and defined by a Reynolds number $\mathcal{R} = 2000$, an equivalence ratio $\Phi = 0.9$, and a volume fraction of 42 percent O_2 in the O_2/CO_2 oxidant. The corresponding pressure spectrum is shown in Fig. 7. In Ditaranto and Hals [19] the spectral distribution of the pressure oscillations is shown in Fig. 7c. From Fig. 1 in [19] the laminar flame speed is $S_L = 0.47$ m/s in the case of 42 percent O_2 in the oxidant.

In the experimental study the flow rate of fuel and oxidant in the attached flame case was 1.3×10^{-4} and 1.65×10^{-3} kg/s, respectively, corresponding to a mean flow velocity in the premixer of 0.42 m/s. With $\mathcal{R} = 2000$ the
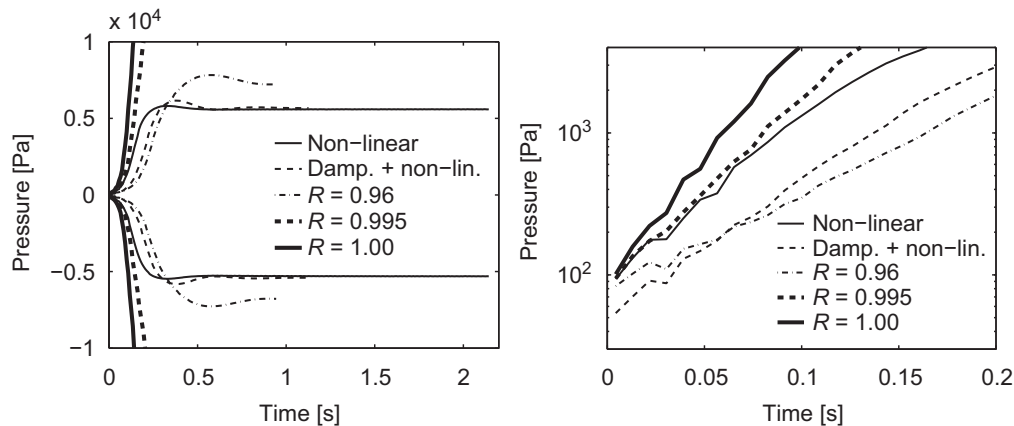
Fig. 8. Limit cycles for simulations using different reflection properties.

attached flame is in the laminar flame regime. Hence, the parameter f_T in Eq. (37) is set to $f_T=1$, i.e., the flame speed is equal to the laminar flame speed.

The observed thermoacoustic instabilities in the flame experiments are governed by statistically stationary limit cycles in which acoustic pressure variations lead to fluctuations in the flow velocity and heat release. The heat release fluctuations, on the other hand, feed back to the acoustic modes at the same frequency. For the oxy-fuel study the limit cycles are controlled by a saturation in the heat release caused by acoustic losses at the outlet. This can be observed in the left graph of Fig. 8, where the envelope of the pressure amplitudes at microphone port 3 of the rig is shown as a function of time for various simulations. We note that when there are no acoustic losses, i.e., when the reflection coefficient $R=1$, the instability grows to infinity. Taking linear acoustic effects into account, we obtain from Eqs. (23) and (47) a reflection coefficient of $R=0.995$ at the dominating frequency $f_0=230$ Hz. The corresponding instability growth is shown by the thick dashed curve in Fig. 8 and displays a slightly smaller growth rate than for the $R=1$ case. By including both nonlinear and radiative losses, the reflection coefficient can be calculated dynamically from Eq. (28). The resulting instability growth is shown by the solid curve denoted "nonlinear" in Fig. 8. If, in addition, viscous damping from the walls of the flame arrestor is taken into account, i.e., the term $F_{f,w}$ in Eq. (12) is non-zero, the growth rate is given by the fairly similar dashed curve denoted "Damp.+nonlin.". (For more details on $F_{f,w}$, see Appendix A). Finally, the dashed-dotted curve in Fig. 8 shows the pressure envelope for a simulation for which $R=0.96$.

From the right graph of Fig. 8 we observe that the thick dashed curve and the solid (thin) curve have very similar slopes for small pressure variations, while for larger pressure amplitudes the nonlinear losses become more and more important and the corresponding solid curve levels out at a much smaller amplitude than the dashed curve. Comparing the simulation results when viscous damping effects were taken into account (dashed curve) with no damping effects implemented (solid curve), we observe that the viscous damping only has little effect on the pressure envelope except for a smaller growth rate initially. The simulation using a reflection coefficient of $R=0.96$ was done as a comparison case and produced a slightly larger pressure amplitude than those indicated for the solid and dashed curves. But the initial growth rate produced by the simpler model produced an initial growth rate that was smaller. From these observations we conclude that it is of crucial importance to the numerical simulations that nonlinear damping through vortex shedding at the combustor outlet is included. The viscous damping at the walls turns out to be of less importance for this specific set-up. One issue to be kept in mind, however, is that the Eqs. (24) and (27) for nonlinear and radiative losses, respectively, were deduced for an open end circular pipe. For the application of a square duct considered here, additional losses due, e.g., to the duct corners might therefore have an impact.

In Fig. 9, the pressure spectra obtained experimentally (thick solid curve) and by numerical simulations (thin dashed and solid curves) are shown. We observe that all the main resonant frequencies of the experiment are well matched by the simulations. In addition, there is a fairly good agreement between the experimental and numerical values of the levels of the resonant peaks of the pressure spectra. However, the levels of the curves in between the resonant modes are lower for the numerical simulations than what was obtained in the experiment. This may be explained by the fact that experimental peaks are generally broader than their numerical counterparts, but the possibility that the difference is due to the 1D approximation cannot be entirely excluded. It is also interesting to note that the peaks of the two numerical pressure spectra are well aligned, except for a small difference for the higher frequency modes.

A final note on the nonlinearities of the quasi-1D model is that by post-processing of the limit cycle behavior it is found that the acoustics is essentially linear, i.e., clear signs of wave steepening are not seen. From Section 3.1.1, it is clearly seen that the reflection coefficients are nonlinear though. Furthermore, during the limit-cycle the flame reaches the level where the strong velocity oscillations bring the flame tip upstream of the sudden expansion and into the slot. As the flame is quenched inside the slot it is indeed the case that the flame does reach nonlinearity. But even before the limit cycle sets in the flame is weakly nonlinear due to flame wrinkling.
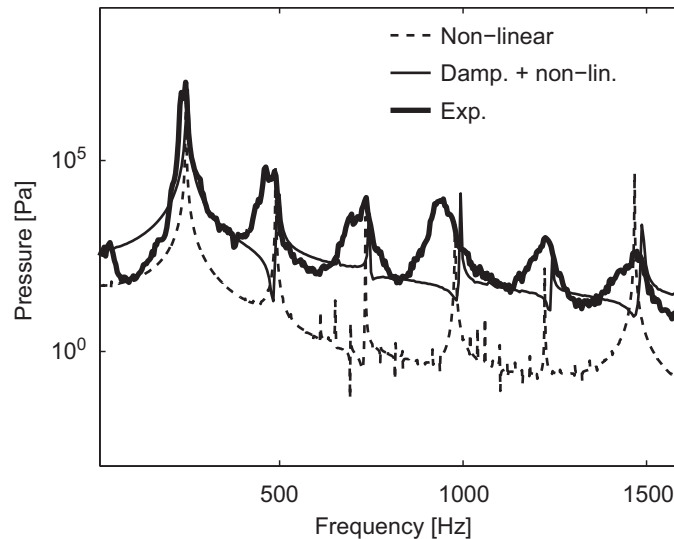
Fig. 9. Experimental and numerical pressure spectra in the combustion chamber at microphone port 3.

6. Conclusion

In this paper we first present the quasi-1D Navier–Stokes and scalar transport equations for a variable cross-section duct. The temperature and species mass equations are closed by expressions for the heat release and the reaction rates obtained from the AFM formulation. The AFM approach has been introduced as a new phenomenological flame model in real space and time for describing attached flames in a 1D geometry of variable cross-section. With the use of the secondary subgrid it is shown that two-dimensional features of a jet entering the combustion chamber is accounted for.

The quasi-1D code is nonlinear and gives the time evolution of real-space quantities. This is in contrast to conventional linear wave-equation models that only give the growth rate of the unstable resonant frequencies, and under the assumption that a linear representation is adequate. Thus, the quasi-1D code is capable of reproducing the nonlinear saturation of the acoustic oscillations, the so-called limit cycle. In order to achieve the correct magnitude of the limit-cycle oscillations, it is crucial to account for the acoustic losses at the open end(s) of a duct. This is done by including the nonlinear effects due to vortex shedding at the sharp bends at the duct exit, in addition to the losses due to acoustic radiation from the open end exit.

The nonlinear code has been validated by first comparing results from using the simplified $n-\tau$ heat release model with corresponding analytical results. The AFM flame model has been validated by producing flame transfer functions and comparing the results with analytical results available in the literature. Finally, the entire code was validated against the oxy-fuel study of Ditaranto and Hals [19] in a sudden expansion burner. With the application of the AFM heat release formulation the numerical simulations were able to reproduce the resonant frequencies of the acoustic pressure spectrum of an oscillating attached flame with high accuracy. In addition, the levels of the resonant peaks were reproduced quite well. From these findings we conclude that the quasi-1D nonlinear Navier–Stokes solver with the AFM formulation is a promising tool for further studies of combustion instabilities in a variety of cases, including jets in variable cross-section ducts or in co-flows.

Acknowledgments

Appendix A. Viscous damping

The acoustic Strouhal number is defined by $\mathrm{Sr}_{ac} = \omega a / \hat{u}$, where ω is the angular frequency of the acoustic oscillations, a is the radius of the pipe, and $\hat{u}$ is the amplitude of the acoustic velocity oscillations. If the acoustic Strouhal number is very small, the boundary layer develops in a time much smaller than the acoustic period. In that case it is a good approximation to assume that the boundary layer is always developed. Following White [31], the viscous force from the walls $F_{f,w}$ then is

$$F_{f,w} = -\tau_w S_P \Delta x, \tag{A.1}$$

where τ_w is the wall shear stress, S_P is the duct perimeter, and Δx is the length of a grid cell. The wall shear stress can be expressed as [31]

$$\tau_w = \tfrac{1}{8} f_D \rho u^2, \tag{A.2}$$

where f_D is the Darcy friction factor. The Darcy friction factor can be approximated with the expression

$$f_D = \frac{64 f_{\mathrm{prof},1}}{\mathcal{R}_{D_h}}, \tag{A.3}$$

for laminar flows. For turbulent flows f_D can be obtained from the relation

$$\frac{1}{\sqrt{f_D}} = 2.0 \log(f_{\mathrm{prof},2} \mathcal{R}_{D_h} \sqrt{f_D}) - 0.8. \tag{A.4}$$

The Reynolds number is based on the hydraulic diameter $D_h = 4A/S_P$, where A is the cross-section of the duct, such that $\mathcal{R}_{D_h} = u D_h / v$. In the above equations, $f_{\mathrm{prof},1}$ and $f_{\mathrm{prof},2}$ are factors whose values are determined by the shape of the duct. Thus, for a flow in a circular pipe $f_{\mathrm{prof},1} = f_{\mathrm{prof},2} = 1$. For a flow between two parallel plates we have $f_{\mathrm{prof},1} = 3/2$ and $f_{\mathrm{prof},2} = 0.64$.

It should be noted that the expression (A.2) is valid only for fully developed flows, see for instance the work by Allam and Åbom [32] for further details. This limitation is most prominent for pipes with large cross-sections, i.e., when the Strouhal number Sr_{ac} is not much smaller than 1. In a flame trap where the viscous damping in general is the largest, however, the given expressions should be relatively good due to the very small cross-sections of the holes. For a more applicable expression for acoustic losses in pipe flows, see the paper by Disselhorst and Wijngaarden [33].

Following Peters et al. [21], for small Helmholtz numbers ka and large shear numbers the damping coefficient due to the viscous boundary layer is given by

$$\alpha = \frac{\omega}{c_0} \left[\frac{1}{\sqrt{2}\,\mathrm{Sh}} \left(1 + \frac{\gamma-1}{\sqrt{\mathrm{Pr}}}\right) + \frac{1}{\mathrm{Sh}^2} \left(1 + \frac{\gamma-1}{\sqrt{\mathrm{Pr}}} - \frac{\gamma(\gamma-1)}{2\mathrm{Pr}}\right) \right], \tag{A.5}$$

where $\mathrm{Sh} = a\sqrt{\omega/v}$ is the shear number and Pr is the Prandtl number. The above expression for α has been established under the assumption of no mean flow in the system. This gives a viscous damping defined as

$$\Delta P' \sim \exp(-\alpha x), \tag{A.6}$$

where $\Delta P'$ is the decrease in the acoustic pressure fluctuations, and x is the distance traveled by the acoustic waves.

References

[1] J.W.S. Rayleigh, *The Theory of Sound*, Macmillan, London, 1896.
[2] S.M. Candel, Combustion instabilities coupled by pressure waves and their active control, *Proceedings of the Combustion Institute* (1992) 1277–1296.
[3] K.R. McManus, T. Poinsot, S.M. Candel, A review of active control of combustion instabilities, *Progress in Energy and Combustion Science* 19 (1993) 1–29.
[4] J.B. Bell, M.S. Day, J.F. Grcar, M.J. Lijewski, J.F. Driscoll, S.A. Filatyev, Numerical simulation of a laboratory-scale turbulent slot burner, *Proceedings of the Combustion Institute* 31 (2007) 1299–1307.
[5] G. Lartigue, U. Meier, C. Brat, Experimental and numerical investigation of self-exited combustion oscillations in a scaled gas turbine combustor, *Applied Thermal Engineering* 24 (2004) 1583–1592.
[6] T. Poinsot, D. Veynante, *Theoretical and Numerical Combustion*, second ed., Edwards, Philadelphia, 2005.
[7] J.J. Keller, Thermoacoustic oscillations in combustion chambers of gas turbines, *AIAA Journal* 33 (1995) 2280–2287.
[8] A.P. Dowling, A kinematic model of a ducted flame, *Journal of Fluid Mechanics* 394 (1999) 51–72.
[9] C. Paschereit, P. Flohr, B. Schuermans, Prediction of combustion oscillations in gas turbine combustors, AIAA paper 2001-0484, 2001.
[10] W. Polifke, A. Poncet, C.O. Paschereit, K. Döbbeling, Reconstruction of acoustic transfer matrices by instationary computational fluid dynamics, *Journal of Sound and Vibration* 245 (2001) 483–510.
[11] A.M. Annaswamy, M. Fleifil, J.P. Hathout, A.F. Ghoniem, Impact of linear coupling on the design of active controllers for the thermoacoustic instability, *Combustion Science and Technology* 128 (1997) 131–180.
[12] A. Fichera, A. Pagano, Application of neural dynamic optimization to combustion-instability control, *Applied Energy* 83 (2006) 253–264.
[13] F.E.C. Culick, Nonlinear behaviour of acoustic waves in combustion chambers—I, *Acta Astronautica* 3 (1976) 715–734.
[14] F.E.C. Culick, Nonlinear behaviour of acoustic waves in combustion chambers—I, *Acta Astronautica* 3 (1976) 735–757.
[15] R. Rook, Acoustics in Burner Stabilised Flames, Ph.D. Thesis. Eindhoven University of Technology, 2001.
[16] J.E. Cohen, B.E. Wake, D. Choi, Investigation of instabilities in a lean, premixed step combustor, *Journal of Propulsion and Power* 19 (2003) 81–88.
[17] D. Prasad, J. Feng, Thermoacoustic stability of quasi-one-dimensional flows—part I: analytical and numerical formulation, *Journal of Turbomachinery* 126 (2004) 637–644.
[18] D. Prasad, J. Feng, Thermoacoustic stability of quasi-one-dimensional flows—part II: application to basic flows, *Proceedings of ASME Turbo Expo 2004*, GT2004-53945, Vienna, Austria, June 2004.
[19] M. Ditaranto, J. Hals, Combustion instabilities in sudden expansion oxyfuel flames, *Combustion and Flame* 146 (2006) 493–512.
[20] H. Levine, J. Schwinger, On the radiation of sound from an unflanged circular pipe, *Physical Review* 73 (1948) 383–404.
[21] M.C.A.M. Peters, A. Hirschberg, A.J. Reijnen, A.P.J. Wijnands, Damping and reflection coefficient measurements for an open pipe at low Mach and low Helmholtz numbers, *Journal of Fluid Mechanics* 256 (1993) 499–534.
[22] L. Boyer, J. Quinard, On the dynamics of anchored flames, *Combustion and Flame* 82 (1990) 51–65.
[23] F. Baillot, D. Durox, R. Prud'Homme, Experimental and theoretical study of a premixed vibrating flame, *Combustion and Flame* 88 (1992) 149–168.
[24] M. Fleifil, A.M. Annaswamy, Z.A. Ghoneim, A.F. Ghoniem, Response of a laminar premixed flame to flow oscillations: a kinematic model and thermoacoustic instability results, *Combustion and Flame* 106 (1996) 487–510.
[25] T. Schuller, D. Durox, S. Candel, A unified model for the prediction of laminar flame transfer functions: comparisons between conical and V-flame dynamics, *Combustion and Flame* 134 (2003) 21–34.

[26] S. Ducruix, D. Durox, S. Candel, Theoretical and experimental determinations of the transfer function of a laminar premixed flame, *Proceedings of the Combustion Institute* 28 (2000) 765–773.

[29] W. Polifke, C. Lawn, On the low-frequency limit of flame transfer functions, *Combustion and Flame* 151 (2007) 437–451.

[30] P.O.A.L. Davies, J.L. Bento Coelho, M. Bhattacharya, Reflection coefficients for an unflanged pipe with flow, *Journal of Sound and Vibration* 72 (1980) 543–546.

[31] F.M. White, *Fluid Mechanics*, fifth ed.,McGraw-Hill, New York, 2003.

[32] S. Allam, M. Åbom, Investigation of damping and radiation using full plane wave decomposition in ducts, *Journal of Sound and Vibration* 292 (2006) 519–534.

[33] J.H.M. Disselhorst, L. van Wijngaarden, Flow in the exit of open pipes during acoustic resonance, *Journal of Fluid Mechanics* 99 (1980) 293–319.